

# Intracellular Dynamic Assembly of Deep-Red Emitting Supramolecular Nanostructures Based on the Pt...Pt Metallophilic Interaction

Xue-Quan Zhou, Maria Mytiliniou, Jonathan Hilgendorf, Ye Zeng, Panagiota Papadopoulou, Yang Shao, Maximilian Paradiz Dominguez, Liyan Zhang, Marcel B. S. Hesselberth, Erik Bos, Maxime A. Siegler, Francesco Buda, Albert M. Brouwer, Alexander Kros, Roman I. Koning, Doris Heinrich, and Sylvestre Bonnet\*

Many drug delivery systems end up in the lysosome because they are built from covalent or kinetically inert supramolecular bonds. To reach other organelles, nanoparticles hence need to either be made from a kinetically labile interaction that allows re-assembly of the nanoparticles inside the cell following endocytic uptake, or, be taken up by a mechanism that short-circuits the classical endocytosis pathway. In this work, the intracellular fate of nanorods that self-assemble via the Pt...Pt interaction of cyclometalated platinum(II) compounds, is studied. These deep-red emissive nanostructures (638 nm excitation, ≈700 nm emission) are stabilized by proteins in cell medium. Once in contact with cancer cells, they cross the cell membrane via dynamin- and clathrin-dependent endocytosis. However, time-dependent confocal colocalization and cellular electron microscopy demonstrate that they directly move to mitochondria without passing by the lysosomes. Altogether, this study suggests that Pt...Pt interaction is strong enough to generate emissive, aggregated nanoparticles inside cells, but labile enough to allow these nanostructures to reach the mitochondria without being trapped in the lysosomes. These findings open new venues to the development of bioimaging nanoplatforms based on the Pt...Pt interaction.


## 1. Introduction

The metallophilic M...M interaction, which is based on d orbital overlap, has been described for planar  $d^8$  and  $d^{10}$  metals, such as gold(I), nickel(II), palladium(II), and platinum(II) complexes.<sup>[1]</sup> It affords fascinating supramolecular aggregated systems with unique optical properties such as “organic” light-emitting diodes or biosensors.<sup>[2–4,5]</sup> The emissive properties arising when the Pt...Pt interaction takes place are attributed to the low-energy metal-centered phosphorescence ( $^3MC$ ), metal-metal-to-ligand charge-transfer ( $^3MMLCT$ ) or ligand-to-metal-metal charge-transfer ( $^3LMMCT$ ) transitions, which also generate red-shifted absorption or excitation bands in the visible or near-UV regions versus monomer bands.<sup>[5,6]</sup> These bands are attributed to the low HOMO–LUMO

X.-Q. Zhou, J. Hilgendorf, Y. Zeng, P. Papadopoulou, Y. Shao, L. Zhang, F. Buda, A. Kros, S. Bonnet  
Leiden Institute of Chemistry  
Universiteit Leiden  
Einsteinweg 55, Leiden 2333 CC, Netherlands  
E-mail: bonnet@chem.leidenuniv.nl

M. Mytiliniou, M. B. S. Hesselberth, D. Heinrich  
Leiden Institute of Physics  
Huygens-Kamerlingh Onnes Laboratory  
Universiteit Leiden  
Leiden 2300 RA, The Netherlands

M. P. Dominguez, A. M. Brouwer  
Molecular Photonics Group  
Van't Hoff Institute for Molecular Sciences (HIMS)  
Universiteit van Amsterdam  
Science Park 904, Amsterdam 1098 XH, Netherlands

 The ORCID identification number(s) for the author(s) of this article can be found under <https://doi.org/10.1002/adma.202008613>.

© 2021 The Authors. Advanced Materials published by Wiley-VCH GmbH. This is an open access article under the terms of the Creative Commons Attribution-NonCommercial License, which permits use, distribution and reproduction in any medium, provided the original work is properly cited and is not used for commercial purposes.

E. Bos, R. I. Koning  
Department of Cell and Chemical Biology  
Leiden University Medical Center  
Eindhovenweg 20, Leiden 2333 ZC, The Netherlands

M. A. Siegler  
Department of Chemistry  
Johns Hopkins University  
Baltimore, MD 21218, USA

A. M. Brouwer  
Materials Department  
Advanced Research Center for Nanolithography  
Science Park 106, Amsterdam 1098 XG, The Netherlands

D. Heinrich  
Institute for Bioprocessing and Analytical Measurement Techniques  
Rosenhof, 37308 Heilbad Heiligenstadt, Germany

D. Heinrich  
Faculty for Mathematics and Natural Sciences  
Ilmenau University of Technology  
98693 Ilmenau, Germany

D. Heinrich  
Fraunhofer Attract 3DNanoCell  
Fraunhofer Institute for Silicate Research ISC  
97082 Würzburg, Germany

DOI: 10.1002/adma.202008613

gap arising when platinum(II) centers come close enough for their  $d_{z^2}$  orbitals to interact; this interaction is typically facilitated by  $\pi$ - $\pi$  stacking of the ligands bound to platinum, which counter-balance the electrostatic repulsion exerted by the positively charged metal centers.<sup>[7]</sup> Overall, and as demonstrated in two-photon imaging,<sup>[8]</sup> red light absorption and deep-red luminescence are both particularly important for intracellular imaging and phototherapeutic compounds, as low-energy light penetrates further into tissues and is less harmful to cells than high-energy visible or ultraviolet light.<sup>[9]</sup>

Independently from their ability to engage into metallophilic interaction, phosphorescent platinum complexes show several advantages for live cell imaging, compared with organic dyes, such as large Stokes shift, reduced photobleaching, and long excited state lifetimes.<sup>[3,10–12]</sup> In parallel, the clinical success of cisplatin has stimulated research toward new platinum-based anticancer drugs and bioinorganic applications of platinum-organic compounds.<sup>[13,14]</sup> Many reports focus on pincer-like platinum complexes based on tridentate polypyridyl ligands because of their tunable photophysical properties, the existence of various mechanisms inducing cytotoxicity, and supramolecular assembly derived from the Pt...Pt metallophilic interaction.<sup>[7,14,15]</sup> Che et al. reported a series of complexes generating supramolecular polymers based on the Pt...Pt interaction which were shown capable of pH-dependent emission in the lysosome of cells.<sup>[11]</sup> The role of proteins in the self-assembly of Pt compounds is very diverse; for example, Cola et al. reported that cell medium prevented some platinum complexes to be internalized by the cells.<sup>[10]</sup> Overall, little is known about the morphology of supramolecular polymers based on the Pt...Pt interaction in cell medium or inside cells, their mechanism of cellular uptake, and the dynamics of their intracellular distribution.

These questions have become particularly relevant because of the emergence of nanomaterials as functional delivery platforms for the imaging and therapy of cancer.<sup>[16,17]</sup> Many types of organic and inorganic theranostic nanosystems have been developed, derived from, for example, lipid-based nanoparticles, polymers, lanthanide fluorides, or silica nanoparticles.<sup>[17,18]</sup> Endocytosis is considered to be the major cellular uptake mechanism for nanoparticles, as a consequence of which they typically end up in the endosome or lysosome.<sup>[19]</sup> The lysosome, in particular, is responsible for the digestion of extracellular substances, and it generates for this aim abundant hydrolytic enzymes and an acidic environment, which limits many nano-drug delivery systems by preventing drug release into the cytosol.<sup>[20]</sup> Thus, nanoparticles capable of endo-lysosomal escape are of great interest. In this work, we demonstrated that self-assembled nanoparticles based on Pt...Pt interaction can move from the cell membrane to the mitochondria directly, with exceptional uptake efficiency, and without the assistance of the lysosomes. These nanoparticles were built from a molecularly well-defined cyclometalated platinum complex, which makes these nanomaterials particularly easy to prepare in a reproducible manner. Because of the aggregation-induced red absorption and deep-red emission of these nanostructures, their low photobleaching, and the high electron density generated by the platinum centers, it was possible to monitor in cells their morphology, fate, and dynamic reorganization by a combination of confocal microscopy, cell electron microscopy, and flow

cytometry, effectively demonstrating cellular uptake by endocytosis, endosomal escape, and relocation into the mitochondria.

## 2. Results

Two isomeric complexes ([PtMeL<sup>1</sup>]OAc ([1]OAc) and [PtMeL<sup>2</sup>]OAc ([2]OAc, Figure 1) were prepared by cyclometalation of the known tetradentate ligands HMeL<sup>1</sup> and HMeL<sup>2</sup>,<sup>[21]</sup> using platinum(II) acetylacetonate in boiling acetic acid. The compounds [1]<sup>+</sup> and [2]<sup>+</sup> differ by the position of the platinum-carbon bond: in [1]<sup>+</sup>, it is closer to the bridging NMe group than in [2]<sup>+</sup> (see full chemical structural analysis in Figures S1–S4, Supporting Information). The <sup>1</sup>H NMR spectra obtained for each complex were different at low (2 mg mL<sup>-1</sup> MeOD) versus high (7 mg mL<sup>-1</sup> MeOD) concentration (Figure S5, Supporting Information), which suggested some form of supramolecular assembly in this solvent. The crystal structure of [2]PF<sub>6</sub> confirmed this tendency: The crystal packing of [2]PF<sub>6</sub> (Figure 1b) clearly identified one short (3.3216(5) Å) and one long (4.2572(6) Å) intermolecular Pt...Pt distance. The short Pt...Pt distance also corresponded to short distances between the aromatic rings of the parallel cyclometalated ligand (the shortest distance around 3.5 Å), demonstrating strong  $\pi$ - $\pi$  stacking as well. Altogether the crystal suggested the formation of supramolecular dimers in the solid state.

According to density functional theory (DFT) and time-dependent density functional theory calculations (TDDFT) run at the PBE0/TZP/COSMO level for both monomolecular complexes in water, the calculated HOMO–LUMO transition of [1]<sup>+</sup> is at much lower energy (441 nm) than that of [2]<sup>+</sup> (375 nm, Figure S6a, Supporting Information). As the HOMO is based on the lone pair of the NMe bridge, and the LUMO is essentially located on the bipyridine part of the ligand, the HOMO in [1]<sup>+</sup> is more destabilized by the closer, electron-rich cyclometalated bond, than the HOMO in [2]<sup>+</sup>, while both bpy-based LUMOs are essentially at the same energy level. The dimers of complexes were also modeled by DFT. According to these calculations, dimers form despite the electrostatic repulsion exerted by the monocationic complexes. Their HOMO is composed of the two  $d_{z^2}$  orbitals on the platinum centers interacting in an antibonding fashion, with an additional contribution from  $\pi$  orbitals of the ligands (Figure 1c). The calculated Pt...Pt distance was short (3.34 Å for [1]<sup>+</sup> and 3.26 Å for [2]<sup>+</sup>), confirming that in such dimers the metallophilic interaction is strong, and occurs as a result of a combination of  $d_{z^2}$  axial overlap and  $\pi$ - $\pi$  stacking. Besides, the HOMO–LUMO energy gaps of both complexes significantly decreased in the dimer state compared with the monomer (Figure S6, Supporting Information), especially for [2]<sup>+</sup>, from 4.13 eV (monomer) to 3.39 eV (dimer). Further TDDFT calculation demonstrated that the dimer of both complexes shows a lower-energy absorption band than their monomer, which can be attributed to a transition from the  $\sigma^*$  orbital on the Pt...Pt axis to  $\pi^*$  ligand-based orbitals, corresponding to an MMLCT excited state. These results indicated that the aggregates of these complexes might be excited at a longer wavelength than the monomers.

The short Pt...Pt distance found in the solid state stimulated us to look for signs of the metallophilic Pt...Pt interaction in

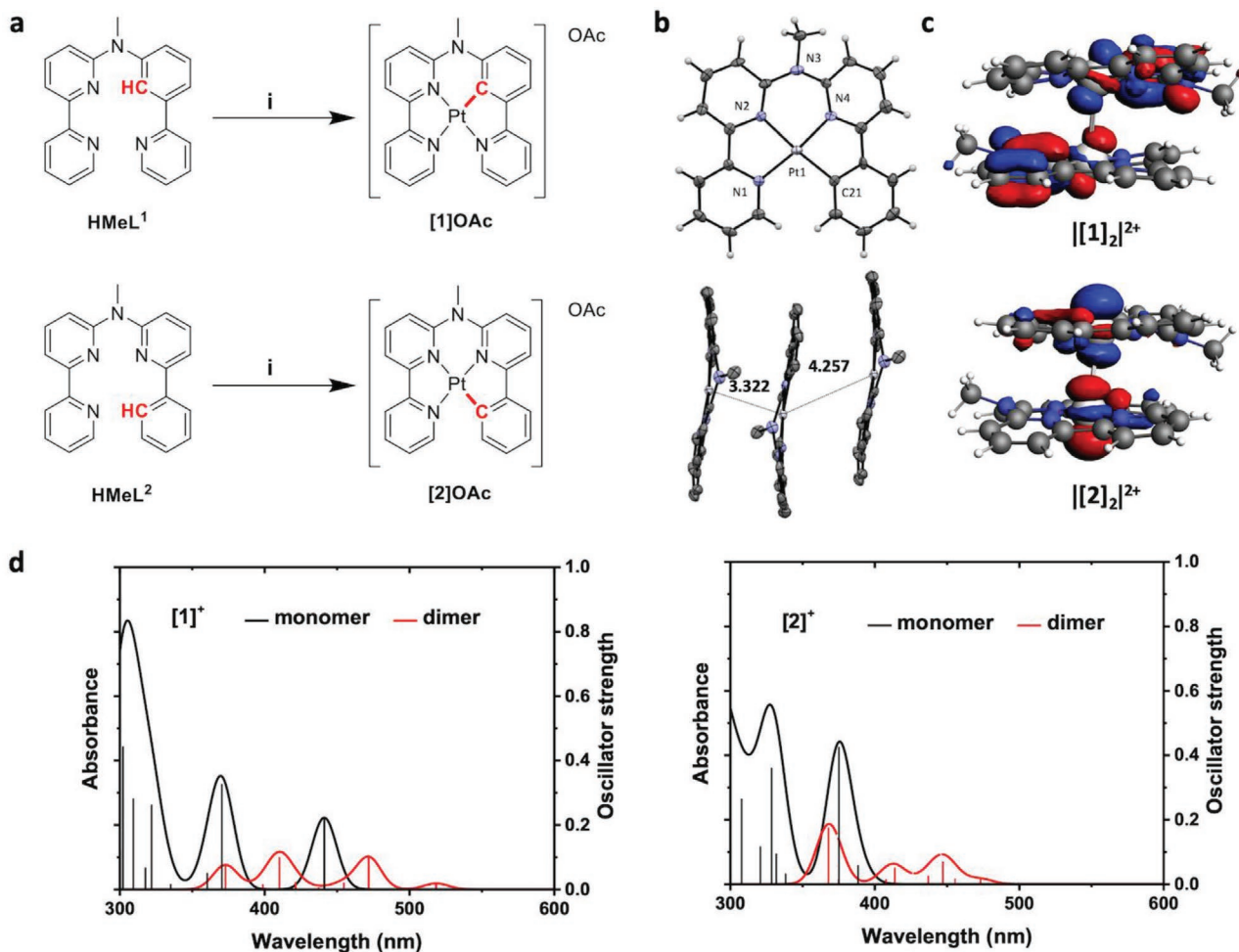


**Figure 1.** a) Synthesis of [1]OAc and [2]OAc. Reaction condition: i) Platinum(II) acetylacetonate (1 equiv.), tetrabutylammonium acetate, CH<sub>3</sub>COOH, N<sub>2</sub>, 135 °C, 6 days; 32% yield for [1]OAc and 93% yield for [2]OAc. b) Displacement ellipsoid plot (50% probability level) and packing of [2]PF<sub>6</sub> at 110(2)K. Element color code: gray = C, blue = N, white = Pt and H; anion has been omitted for clarity; Pt...Pt distances are given in Å. c) HOMO of [1]<sub>2</sub><sup>2+</sup> and [2]<sub>2</sub><sup>2+</sup> showing the d<sub>z<sup>2</sup></sub> overlap, calculated by DFT at the PBE0/TZP/COSMO level in water. Element color code: gray = C, blue = N, white = Pt and H. d) Excitation spectra of [1]<sup>+</sup> and [2]<sup>+</sup> in the monomeric and dimeric states according to TDDFT calculations.

solution. Emission and absorption spectroscopy studies were hence undertaken at a concentration of 50 μM in methanol or in aqueous solutions. In methanol, both complexes were highly soluble, and spectroscopically speaking, comparatively high-energy absorption (451 nm or lower) and emission maxima (604 for [1]OAc and 556 and 591 nm for [2]OAc, see Figure 2a; Table S6, Supporting Information) were found, which suggested an absence of metalophilic interaction and hence monomeric species. The distinct absorption of both isomers in MeOH can be attributed to their different HOMO–LUMO gap (Figure S6a, Supporting Information), which critically depends on the proximity between the Pt–C bond and the non-bonding electron pair on the NMe bridge.<sup>[22]</sup> While in aerated methanol (50 μM), the luminescence of both complexes was weak, as characterized by low quantum yields (below 0.0015, Table S6, Supporting Information); in degassed methanol, their luminescent quantum yield increased ≈2–4 times (still remaining lower than 0.005), which demonstrated the triplet nature of the excited states of these monomers, but also suggested that O<sub>2</sub> is not so

good at quenching the monomer emission. This observation was confirmed by the singlet oxygen generation quantum yield, which was moderate in aerated methanol solution (φ<sub>Δ</sub> = 0.44 for [1]OAc, 0.11 for [2]OAc). The photodynamic properties of both complexes were hence limited as monomers in methanol. In frozen MeOH/EtOH mixtures (77 K, Figure S8b, Supporting Information), the phosphorescence quantum yield was further increased by a factor >20 for [1]OAc and >100 for [2]OAc (see Table S6, Supporting Information), suggesting possible intermolecular (triplet–triplet annihilation) or intramolecular (vibrational) quenching routes at room temperature. Limited quenching by O<sub>2</sub> was confirmed by luminescent lifetime measurements (Table S6 and Figure S8, Supporting Information): for both isomers, biexponential decay was observed, but considering the very low phosphorescence intensity, we interpret the short component τ<sub>1</sub> as a consequence of scattered light from the laser pulse; the longer lifetime τ<sub>2</sub>, which we interpret as that of the Pt complex, increased by a factor of 2–4 upon degassing (e.g., from 150 to 602 ns for [1]OAc and from 33 to 71 ns

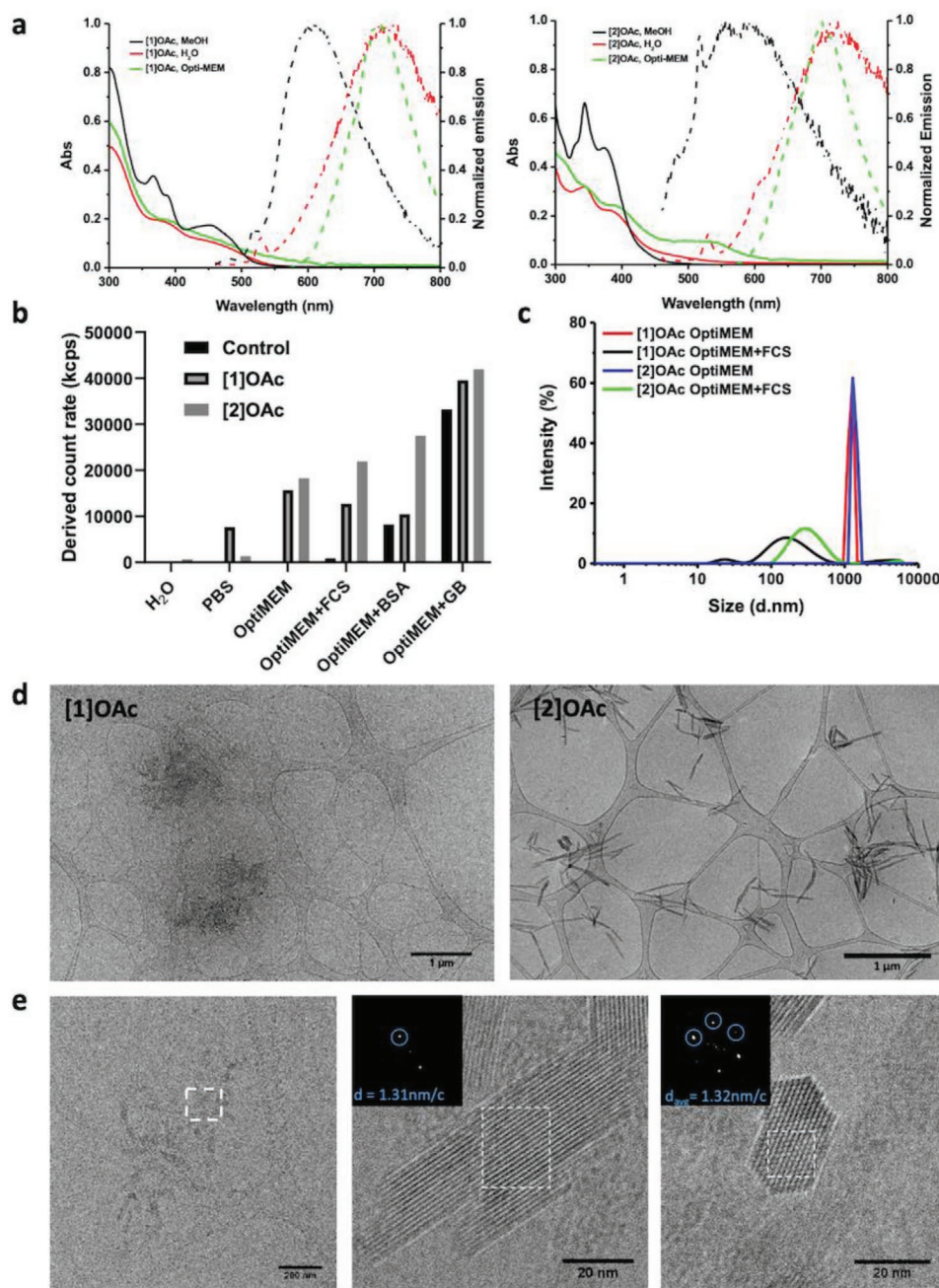


**Figure 2.** a) The absorption spectra (solid lines, 50  $\mu\text{M}$ ) and the emission spectra (dashed lines, with excitation at 450 nm, absorption set at 0.1) of [1]OAc and [2]OAc in aerated methanol (black), water (red), and Opti-MEM complete medium (green). b) DLS mean count rate (kcps) of solutions of [1]OAc or [2]OAc in water (50  $\mu\text{M}$ ), PBS, Opti-MEM, Opti-MEM with fetal calf serum (FCS), serum albumin (BSA), and globulin (GB). c) Size distribution of complexes [1]OAc and [2]OAc (50  $\mu\text{M}$ ) in Opti-MEM medium with and without FCS (X-axis is the hydrodynamic diameter in nm, Y-axis is relative intensity in %). d) Cryo-EM images of [1]OAc–[2]OAc in Opti-MEM complete medium (50  $\mu\text{M}$ ). e) High-resolution cryo-EM images of [1]OAc in Opti-MEM complete medium (50  $\mu\text{M}$ ); insert: average repeating distance as indicated by FFT (nm per repeating cycle).

for [2]OAc, see Table S6, Supporting Information). According to TDDFT calculation on the monomeric cations [1]<sup>+</sup> and [2]<sup>+</sup> and to data above, the weak emission in methanol can be assigned to triplet ligand-to-ligand charge-transfer (<sup>3</sup>LLCT) transitions with a small triplet metal-to-ligand charge-transfer (<sup>3</sup>MLCT) character.

The spectroscopic properties of the complexes were quite different in aqueous media. Two types of solutions were

investigated: either pure water, or Opti-MEM complete cell-growing medium, which contained 2.5% V/V fetal calf serum (FCS). In pure water, moderate bathochromic shifts of the absorption maxima of both compounds were observed, suggesting that low-energy <sup>3</sup>MMLCT states derived from the Pt...Pt interaction may occur (Figure 2a).<sup>[2,3]</sup> The emission of both compounds was also strongly red-shifted, with maxima at 655 and 691 nm for [1]OAc, 651, and 687 nm for [2]OAc. In

principle, these red-shifted bands may be attributed either to excimers or to mixed <sup>3</sup>MLCT and <sup>3</sup>MMLCT transitions emission from a mixture of monomers and oligomers or polymers self-assembled via the metallophilic interaction. However, the fact that the deep-red emission strongly resembled to the emission of the complexes in the solid state (Figure S9, Supporting Information), concluded more surely to the hypothesis of self-assembly, which was also confirmed by DLS and cryo-electron microscopy studies (see below). Interestingly, in water the phosphorescence intensity and lifetimes remained essentially constant whether oxygen was present or not (Table S6 and Figure S8), suggesting that self-assembly was strongly modifying the ability of the excited states of these Pt complexes to be quenched by O<sub>2</sub>. The long component of the lifetime  $\tau_2$  was also significantly shorter in pure water for the supramolecular oligo-/poly-mers than in MeOH for the monomer (e.g., 32 ns vs 150 ns for [1]OAc, 8.8 vs 33 ns for [2]OAc in air, see Table S6, Supporting Information). In Opti-MEM complete (50  $\mu$ M), the bathochromic shift of the absorption bands of both complexes was increased beyond that observed in pure water; for [2]OAc a new absorption maximum even appeared at 540 nm. For both complexes, deep-red emission was observed in Opti-MEM complex (705 nm for [1]OAc, 699 nm for [2]OAc), which matched well with that of the complexes in the solid state (Figure S9, Supporting Information), and was hence, the clear spectroscopic signature of <sup>3</sup>MMLCT transitions arising from Pt...Pt supramolecular polymers.<sup>[3]</sup> As a note, [2]OAc showed a much higher emission intensity in the solid state than [1]OAc, which might be partially ascribed to the shorter Pt...Pt distance of [2]OAc and its comparatively stronger Pt...Pt interaction calculated by DFT (Pt...Pt distance: 3.34 Å for [1]\* and 3.26 Å for [2]\*). Besides the absorbance and emission properties, we found that the two platinum complexes showed negligible singlet oxygen generation quantum yields (Table S6 and Figure S7, Supporting Information) both in the monomeric (CD<sub>3</sub>OD solution) and aggregated (Opti-MEM complete medium) states. These low values suggest weak photodynamic properties for the supramolecular aggregates formed by [1]OAc and [2]OAc in cell-growing media, in strong contrast with their palladium analogues.<sup>[21]</sup>

Overall, the spectroscopic results described above suggested the formation of aggregates in aqueous solution via the Pt...Pt metallophilic interaction. However, these were only indirect proofs and the morphology of the aggregates were not known; meanwhile, the distinct emission maxima in Opti-MEM versus pure water also suggested that other components of cell medium, such as salts, proteins, or small biomolecules, may play a role in the aggregation process as well. To study this question in more details, the size and number of nanoparticles obtained with [1]OAc and [2]OAc were investigated via dynamic light scattering (DLS) and transmission electron microscopy (TEM) in water, PBS, and Opti-MEM solution in the presence of different added proteins, that is, fetal calf serum (FCS), bovine serum albumin (BSA), or globulin (GB). In pure water, very few nanoparticles were detected by DLS (derived count rate (kcps) < 700, Figure 2b), compared to PBS where the complexes showed significant aggregation (higher kcps values, kcps = 7627 and 1373 for [1]OAc and [2]OAc, respectively, Figure 2b), indicating that the addition of salts might stimulate the self-assembly of the complexes. However, the time-evolution of the

absorption spectra of PBS solution of the complexes showed a gradual decrease (Figure S11, Supporting Information), suggesting slow precipitation (i.e., colloidal instability) in such conditions. When dissolved in the Opti-MEM medium with or without FCS, the size of the particles exhibited a large difference. DLS measurements showed the presence of 100–500 nm nanoaggregates in Opti-MEM solutions containing FCS (v/v 2.5%, Opti-MEM complete), and of much larger aggregates (>1000 nm) indicative of precipitation in Opti-MEM medium deprived of FCS, suggesting that the proteins present in FCS may play a key role in the stabilization of the nano-sized aggregates in solution (Figure 2b,c; Figure S11, Supporting Information). These results were confirmed by UV-vis spectroscopy: in Opti-MEM complete solution, the two platinum complexes showed a gradual increase in light absorption with time, which we attributed to increased light scattering due to the formation of nanoaggregates that remained in solution. Reversely, the absorption dramatically decreased in time when no FCS was present in medium, which is consistent with the hypothesis of fast precipitation (Figure S13, Supporting Information). When either pure BSA (50 g L<sup>-1</sup>) or pure globulin (30 g L<sup>-1</sup>), that is, the two main proteins present in FCS, were dissolved in Opti-MEM medium and added to solutions of the complexes (50  $\mu$ M), DLS indicated stabilization of the aggregates in solution by keeping the size of the aggregates lower than 1000 nm, demonstrating that both proteins play a key factor in the stabilization of the nanoaggregates of these complexes (Figure 2b; Figure S11, Supporting Information).

Of course, the hydrodynamic size indicated by standard DLS measurements is an average size calculated under the assumption that the nanoaggregates have a spherical shape, which may not be correct. The polydispersity indices obtained in the presence of the nanostructures were always very high (Table S7, Supporting Information), which was a sign of a misfit between the traditional spherical model used for DLS interpretation, and the real morphology of the nanostructures obtained with [1]OAc and [2]OAc, which is more elongated. In order to study their real shape, TEM images were first realized. These images (Figure S14, Supporting Information) suggested that the aggregates in Opti-MEM complete may be a mixture of irregular round nanoparticles with an average size of 56 nm for [1]OAc and 40 nm for [2]OAc, mixed with nanorod structures of 20 nm thickness. TEM also showed that [2]OAc resulted in more concentrated nanorod generation than [1]OAc, which might be attributed to the stronger Pt...Pt interaction (see above). A clear signature for Pt was detected by energy-dispersive X-ray spectroscopy of these nanoaggregates (EDX, see Figure S15a, Supporting Information), suggesting that the platinum complexes were indeed involved in nanoaggregate formation. A more thorough EDX measurement for the nanoparticles and nanorods of [2]OAc further revealed that Pt, C, and Na were the main elements in the nanoparticles (Figure S15b, Supporting Information), suggesting that the salts present in Opti-MEM medium were also probably involved in the formation of these nanostructures.

However, TEM is sub-optimal for determining the structures of self-assembled nanoparticles in solution, since structures are dried during preparation. To alleviate this problem, cryo-EM was carried out, which allows for observing the nanostructures in a vitrified solution state. The cryo-EM images of [1]OAc and

[2]OAc (50  $\mu\text{M}$ , Figure 2d) in Opti-MEM complete medium show clear nanorod structures with a width of  $\approx 30$  nm; specifically, no round particles were observed in cryo-EM images. The nanoparticles of [1]OAc were of smaller dimensions than that of [2]OAc, which matched with the TEM results. Cryo-EM imaging at higher magnifications for the nanoparticles of [1]OAc (Figure 2e), clearly revealed a crystalline structure for the nanorods, characterized by a high contrast hexagonal lattice captured in both  $x$  and  $z$  directions (repeating distance  $\approx 1.3$  nm as indicated by fast Fourier transform). Overall, for both cyclometalated complexes [1]OAc and [2]OAc, the Pt...Pt interaction observed in the solid state triggered, in aqueous solutions containing proteins and salts, self-assembly into deep-red emissive nanorod-like aggregates. The essential role played by the plasma proteins contained in cell-growing media for the stabilization of these self-assembled nanorods at finite, soluble dimensions, suggests that these proteins may be part of the self-assembly. Such “recruitment” of plasma proteins by both platinum complexes distinguishes these NIR-emissive nanostructures from those generated by deliberately mixing amphiphilic platinum complexes and virus capsid proteins,<sup>[23]</sup> or from those stabilized by covalent polymers.<sup>[24]</sup>

Considering the emissive properties of the nanoaggregates of [1]OAc and [2]OAc in serum-containing aqueous solutions, their biological properties in human cancer cell lines were further investigated. Both complexes showed significant cytotoxicity in A549 lung cancer cell lines after 72 h incubation in the dark, with  $\text{EC}_{50}$  values of 10  $\mu\text{M}$  for [1]OAc and 5  $\mu\text{M}$  for [2]OAc, but negligible cytotoxicity in A431 human skin carcinoma, with  $\text{EC}_{50}$  values of 94  $\mu\text{M}$  for [1]OAc and 68  $\mu\text{M}$  for [2]OAc (Figure 3a). None of the complexes showed significant photocytotoxicity under blue light irradiation (455 nm, 5 min, 5.7  $\text{mW cm}^{-2}$ , 1.7  $\text{J cm}^{-2}$ ) in normoxic condition (21%  $\text{O}_2$ , Figure 3a). After 24 h treatment with 5  $\mu\text{M}$  of [1]OAc and [2]OAc, a very high platinum cellular uptake was observed, as measured with ICP-MS in A549 cells and A431 cells, up to  $0.51 \pm 0.03$   $\mu\text{g Pt/million cells}$  (Figure 3b; Table S8, Supporting Information), which is more than 100-fold higher efficiency than that of cisplatin.<sup>[25]</sup> This result gives a strong indication that nanoaggregation can significantly improve metallodrug uptake. The A549 cells treated with 5.0  $\mu\text{M}$  of the platinum complexes for 24 h and imaged by confocal microscopy showed strong deep-red phosphorescence in the 650–750 nm region under 638 nm excitation, which suggested that emissive nanoaggregates similar to those observed in cell-free conditions, are also formed inside the cancer cells (Figure 3c). Interestingly, continued confocal imaging for 48 h (see Figure S16 and Video S1, Supporting Information) demonstrated that the emission of [1]OAc does not photobleach or degrade during that period, even upon cells splitting (Video S2, Supporting Information), and thus, that nanoaggregates formed via Pt...Pt interaction are not only surviving dioxygen and light, but also cell division.

Further colocalization imaging experiments were carried out at 552 nm excitation wavelength, where both complexes show a better absorption compared with 638 nm. A549 cells were first treated with platinum complexes (5  $\mu\text{M}$ ) for 24 h, then co-stained for 15 min with Hoechst 33342 (0.1  $\mu\text{g mL}^{-1}$ ), a nucleus dye for living cells. The confocal images (Figure S17, Supporting Information) showed that [1]OAc-[2]OAc did not localize in the

nucleus. More colocalization experiments were performed with green-emitting dyes for different organelles, such as lysosomes, mitochondria, golgi apparatus, endoplasmic reticulum (ER), and lipid droplets. The overlapping images (Figures S18 and S19, Supporting Information) indicated an anti-correlation of [1]OAc-[2]OAc with the ER, lysosomes and lipid droplets, suggesting they do not stay in such organelles after 24 h treatment. Though the emission of [1]OAc overlapped well with the Golgi apparatus (Pearson's correlation coefficient (PPC) values of 0.5–0.7, see Table S9, Supporting Information),<sup>[26]</sup> the emission characteristics of Golgi dye and metal complexes were significantly different: the former one showed a thread-like emissive pattern, while the platinum complex showed non-consecutive red dots in the cells. Thus it is elusive whether or not [1]OAc is present in the Golgi 24 h after treatment. For [2]OAc, the best co-localization pattern was obtained for the mitochondria, for which color-dependent pixel intensity curves (Figure 4a,b) and high PPC values (0.2–0.6, Table S9, Supporting Information) were obtained. Overall, 24 h after compound addition, [2]OAc emitted primarily from the mitochondria, while the localization of [1]OAc in cells was unclear. Specially, some cells in Figure 4a that did not have intense GFP emission were either cells that had just split and had not enough time to express GFP, or cells where GFP expression was simply low. Thus the co-localization between the platinum(II) complexes and the mitochondria stains were only observed in some of the cells, which is a common problem for vectorized GFP imaging.

Because of their aggregation-induced deep red emission, the cell uptake mechanism of complexes could be monitored via flow cytometry. A549 cells were co-incubated with [1]OAc or [2]OAc (5  $\mu\text{M}$ ) and different cell uptake inhibitors, after which the variations of the relative fluorescent cell populations at 2 h were assessed by FACS.<sup>[27]</sup> The presence of self-assembled nanorods of the complexes in medium inspired us to particularly look into different inhibitors of endocytosis, an active transport mechanism for the uptake of nanoparticles across the cell membrane. Thus we chose a series of endocytosis and active transport inhibitors, including sodium azide ( $\text{NaN}_3$ , active transport inhibitor), pitstop 2 (clathrin-dependent endocytosis inhibitor), dynasore (dynamin-dependent endocytosis inhibitor), nocodazole (phagocytosis inhibitor), and wortmannin (macropinocytosis inhibitor).<sup>[28]</sup> As shown in Figure 4c, nocodazole and wortmannin did not result in inhibition of the relative deep-red fluorescent cell populations, thus excluding the role of phagocytosis and micropinocytosis in the drugs uptake.  $\text{NaN}_3$  showed slight uptake inhibition for both complexes, suggesting that active transport and clathrin-dependent endocytosis are playing an active but limited role in compound uptake. The strongest response was obtained after treatment with dynasore and Pitstop 2, upon which the percentage of emissive cells was dramatically decreased, compared with the control groups only treated with the complexes. Specifically, pitstop 2 showed a more significant uptake inhibition for [1]OAc than [2]OAc, suggesting the different endocytic pathways for the isomeric compounds, while dynasore had an equal and large effect on both compounds. Overall, these data indicated that [1]OAc and [2]OAc enter into cells by dynamin-dependent and clathrin-dependent endocytosis, which is consistent with the hypothesis of uptake as nanoparticles.<sup>[29]</sup>

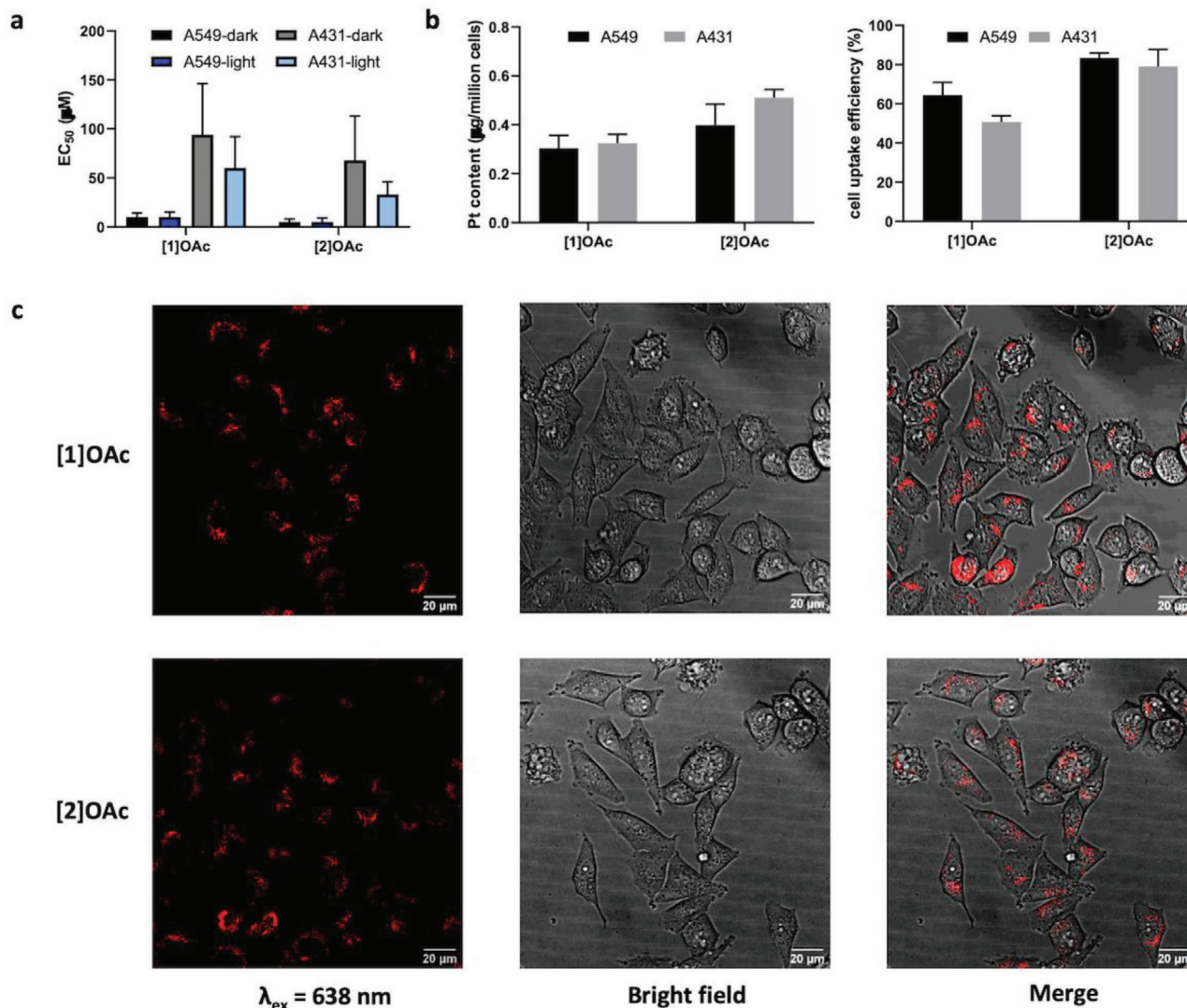


**Figure 3.** a) EC<sub>50</sub> values of [1]OAc or [2]OAc in the dark or under blue light irradiation (455 nm, 5 min, 5.7 mW cm<sup>-2</sup>, 1.7 J cm<sup>-2</sup>). b) Pd content as measured by ICP-MS and cellular uptake efficiency (cellular Pt content/working solution Pt content × 100%) for A549 and A431 cells treated with [1]OAc and [2]OAc (concentration 5 μM) after 24 h incubation. c) Confocal images of A549 cells (scale bar 20 μm) after 24 h treatment with [1]OAc and [2]OAc (5 μM, λ<sub>ex</sub> = 638 nm, λ<sub>em</sub> = 650–750 nm).

Still, these flow cytometry experiments were based on the aggregation-induced deep red emission, and hence only measured internalization of the aggregated particles, but no detection of the essentially non-emissive monomeric platinum complexes, which might be uptaken via energy-independent transport. Thus ICP-MS was used to detect the whole Pt content of A549 cells treated with the Pt complex alone at 37 °C (control), the complex alone at 4 °C, to check passive uptake, or the complex co-incubated with dynasore for 2 h. First, the control cellular uptake 2 h after treatment was ≈ three times lower than 24 h after treatment (see above), suggesting time-dependent cell internalization. Second, as shown in Figure 4d, dynasore inhibited the cellular uptake of the two Pt complexes, matching well with the flow cytometry analysis. At 4 °C, significant cellular uptake inhibition was observed for both complexes, resulting in 53% and 58% reduction of the Pt content for [1]OAc and [2]OAc, respectively (Table S10, Supporting Information), which accounts for the shutting of active uptake

processes at low temperatures. On the other hand, there was still significant Pt uptake at low temperature, which means that not all Pt complexes are taken up by active processes. Overall, these results suggest that more than half of the platinum complexes are internalized in A549 cells by energy-dependent, endocytic transport, while a bit less than half of the metal complexes cross the cell membrane via passive diffusion or energy-independent channels.

As [2]OAc showed increased colocalization with mitochondria after 24 h, and its major internalization mechanism was endocytosis, we engaged into investigating the time evolution of its intracellular colocalization with lysosomes and mitochondria upon uptake. Following 3 h incubation with [2]OAc and fluorescent labeling of the lysosomes and mitochondria, fluorescent images of A549 cells were acquired at time points 3.5, 4.5, 5.0, 5.5, 6.0, 21.0, and 45.0 h (time point zero was set to the time of addition of the compound). Volume-view images of representative cells at 3.5, 6.0, 21.0, and 45.0 h are shown in

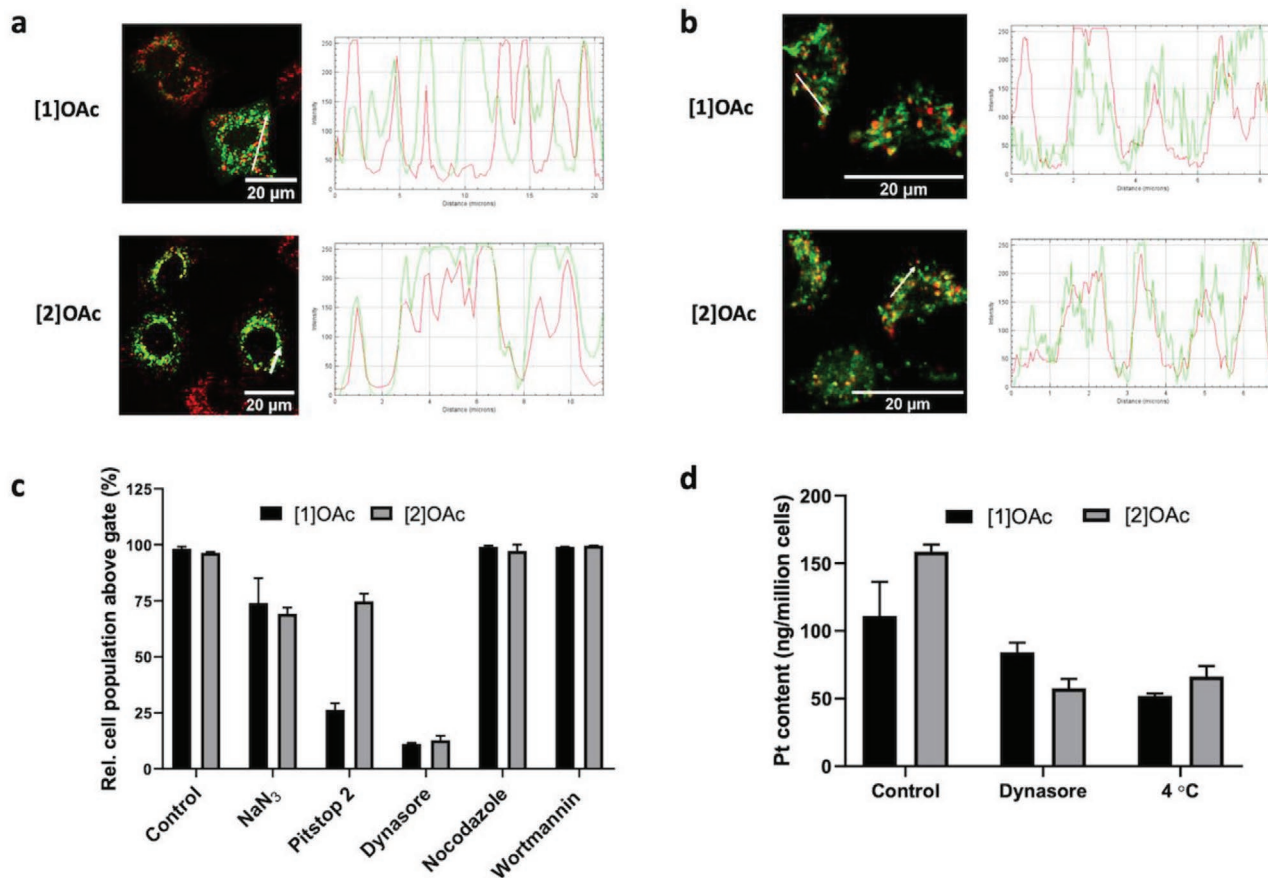


**Figure 4.** Cellular uptake of [1]OAc-[2]OAc in A549 cells after 2 h incubation. a,b) Overlapping images and pixel intensity curves of A549 cells treated with [1]OAc or [2]OAc (red color, 5  $\mu$ M) and a) Mitochondria green fluorescent protein (GFP, green) or b) MitoTracker Green FM (green color). c) Relative fluorescent cell population (%), according to cell flow cytometry (FACS), after treatment of A549 cells with [1]OAc-[2]OAc (5  $\mu$ M) and different cellular uptake inhibitors. d) Pt content, according to ICP-MS analysis, of A549 cells treated with [1]OAc-[2]OAc (5  $\mu$ M) for 2 h at 37  $^{\circ}$ C, without (control) or with dynasore, or at 4  $^{\circ}$ C.

**Figure 5a.** The top row shows the lysosomes (blue), the second row the mitochondria (green), the third row shows the [2]OAc compound (red), and the fourth and fifth row shows the merged phosphorescence of [2]OAc (red) with lysosomes (blue) and mitochondria (green), respectively. Lysosomes phosphorescence increased with incubation time, whereas mitochondria phosphorescence exhibited a peak at 6.0 hours and a subsequent decrease, especially at the time point of 45.0 h. [2]OAc phosphorescence increased at time points 21.0 and 45.0 h, with bigger aggregates clearly distinguishable inside the cells, suggesting that the platinum complex probably aggregates in the cell. An increase in the colocalization of [2]OAc with the mitochondria was observed with increasing time. This observation was confirmed quantitatively by plotting Mander's overlap coefficient versus time (Figure 5b).<sup>[30]</sup> The moderate overlap coefficients of [2]OAc with mitochondria (around 0.5) should be attributed to different factors: i) the motion of the nanoparticles from the cell membrane to mitochondria; ii) the motion of the mitochondria; iii) the aggregation of platinum complexes, which is supramolecular in nature and must hence depend on the environment inside the cell; and iv) possibly, photoinduced emission quenching inside the mitochondria.

Comparatively, colocalization of [2]OAc with the lysosomes (grey circles) was rather low (overlap coefficient below 0.15) for all time points, suggesting limited uptake of the nanoaggregated platinum compound by the lysosomes. However, these results conflict with the typical endocytosis mechanism that usually involves endosomes and lysosomes. This conflict may indicate that [2]OAc traffics to mitochondria directly after dynamin- and clathrin-mediated endocytosis, an endocytotic mechanism that is unusual but was reported recently.<sup>[31]</sup> Alternatively, the accumulation of emissive nanoparticles in the mitochondria at 24 h could also be the result from passive uptake of the compound as monomer, migration to the mitochondria driven by the negative charge of the mitochondrial membrane ([2]<sup>-</sup> is monocationic), and re-assembly due to the increased local concentration of the monomer. The decrease in colocalization of [2]OAc with both the lysosomes and the mitochondria after 45.0 h might be due either to partial degradation of the complex, or to disassembly; this is suggested also by Figure 5c, where the average deep-red fluorescent intensity of [2]OAc per cell shows a slight decrease at 45.0 h, as compared to that at 21.0 h. The mean [2]OAc intensity per cell exhibits an increase after 21.0 h as compared to that for 3.5–6.0 h, as shown in Figure 5c, probably due to the formation of larger



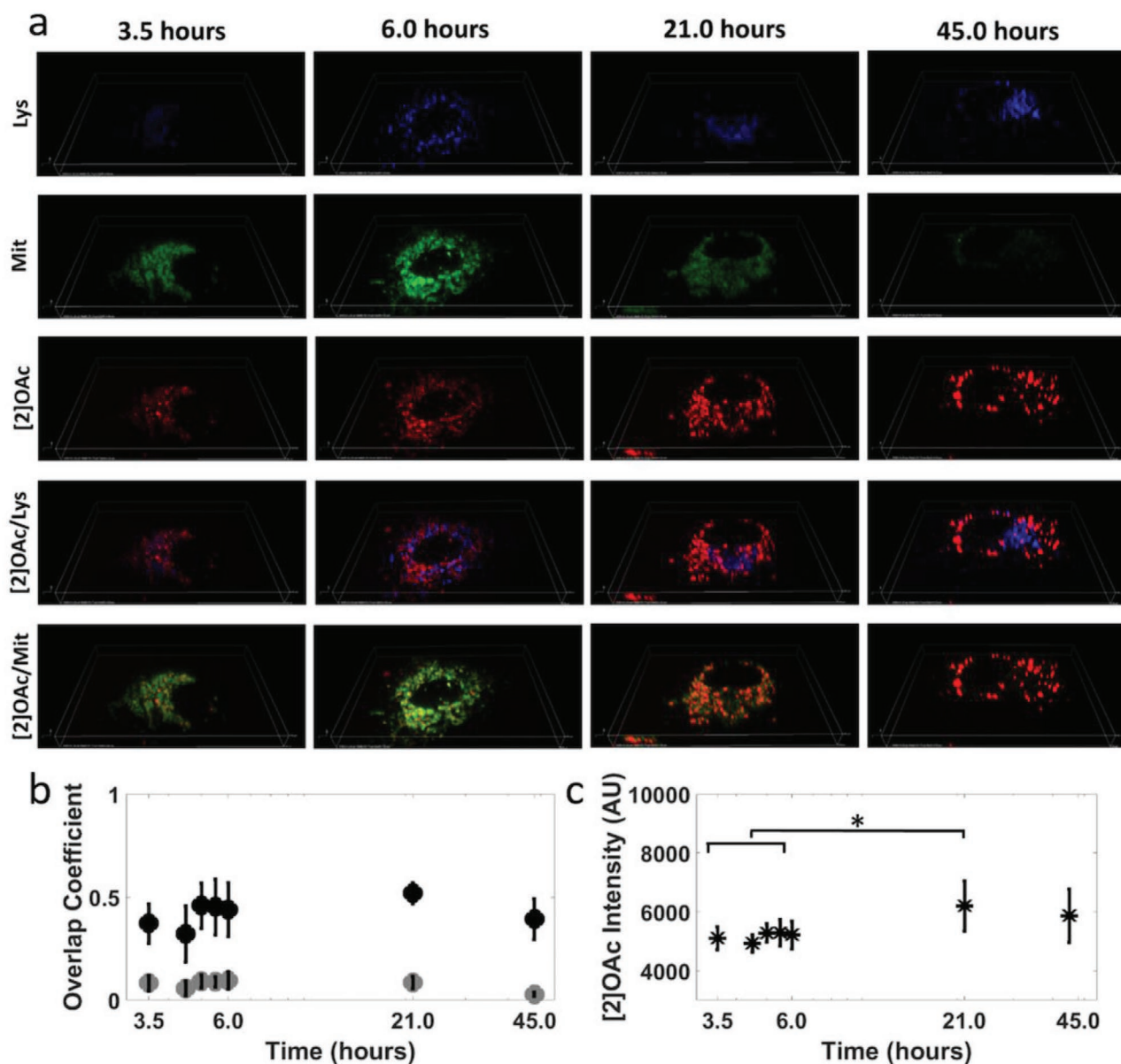


**Figure 5.** a) Fluorescent images of lysosomes (blue, top row), mitochondria (green, second row), [2]OAc (red) (third row), merged [2]OAc with lysosomes (fourth row), and merged [2]OAc with mitochondria (bottom row), at 3.5, 6.0, 21.0, and 45.0 h after 3-h incubation with [2]OAc ( $t = 0-3$  h). b) Quantification of [2]OAc colocalization with lysosomes (grey) or mitochondria (black) at 3.5, 4.5, 5.0, 5.5, 6.0, 21.0, and 45.0 h after 3-h incubation with [2]OAc ( $t = 0-3$  h). Overlap coefficients were calculated using Mander's overlap coefficient (MOC) with the Nikon Nis elements software and are shown as mean values  $\pm$  standard deviations of an average of 8–16 cells per time point. c) [2]OAc mean intensity per cell, at 3.5, 4.5, 5.0, 5.5, 6.0, 21.0, and 45.0 h. Values are shown as means  $\pm$  standard deviations of an average of 6–11 cells per time point. Statistical significance  $p$ -values were calculated using the Wilcoxon statistical test \*  $p \leq 0.05$ .

aggregates. Although the increase is statistically significant, the difference is of the same order of magnitude in the intensity scale (a bit more than 6000 AU for 21.0 h, vs  $\approx$  5000 AU for 3.5–6.0 h), whereas visually it appears more intense (Figure 5a, third row). This observation may be attributed to a non-linear relationship between the phosphorescence intensity observed and the size of [2]OAc aggregates formed.<sup>[32]</sup> Altogether, these data confirmed the accumulation of deep-red emissive aggregates of [2]OAc inside the cellular environment already 3 h after treatment, the limited assistance of lysosomes during

aggregates internalization, and a tendency of the compound to co-localize with the mitochondria.

The limited spatial resolution of confocal microscopy, and the conflicting observations of an endocytosis uptake with limited colocalization with the lysosomes, pushed us to use electron microscopy (EM) imaging to study the fate and morphology of the nanoparticles inside the cells. EM imaging of A549 cells incubated for 3, 5, and 24 h with compound [2]OAc (5  $\mu$ M) was performed. No nanoparticles were observed in the untreated cell control group (Figure S21, Supporting Information). On the

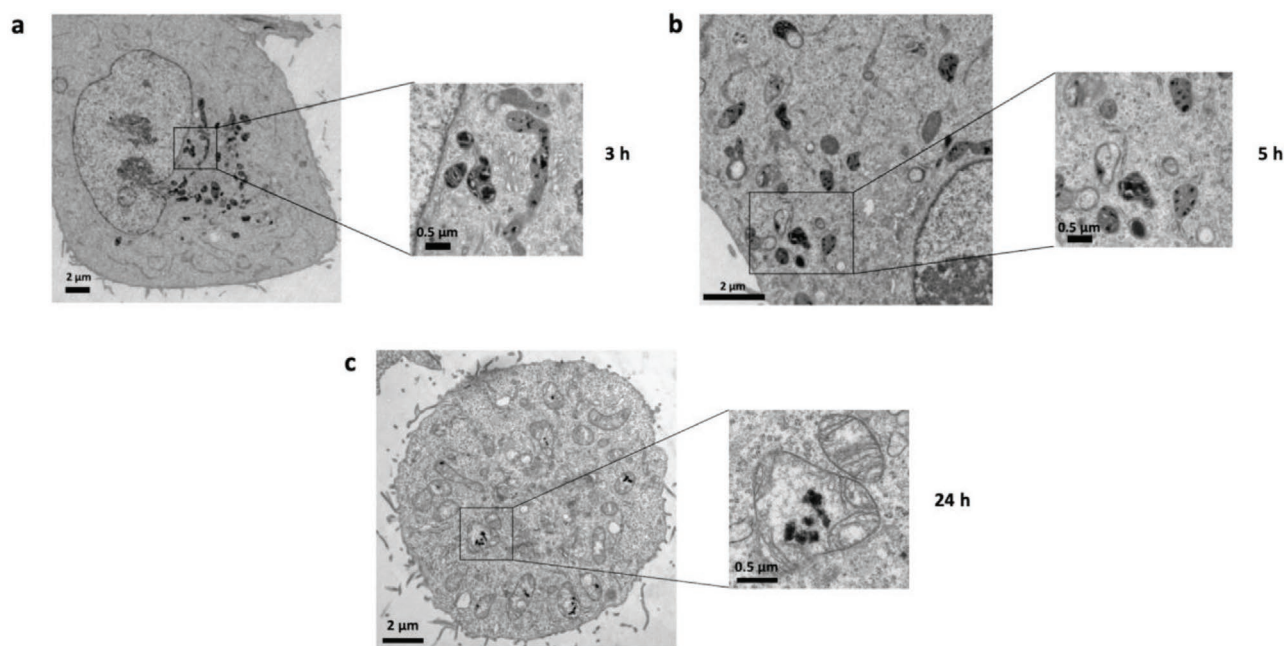


**Figure 6.** EM images of A549 cells 24 h after treatment with [2]OAc (5  $\mu\text{M}$ ) at a) 3 h, b) 5 h, and c) 24 h (scale bar 2 or 0.5  $\mu\text{m}$ ).

other hand, many dark-contrasted spots were observed in the treated cells, indicative of nanoparticles of [2]OAc (Figure 6a–c). These nanoparticles were located in the mitochondria, which is in agreement with the confocal microscopy data. Note that the apparent morphology of nanoaggregates of [2]OAc in the mitochondria of sectioned cells looked like nanoparticles, which seemed different from the nanorod morphology observed in cell-free medium (Figure 2). However, nanorods observed in absence of cells by cryo-EM, are not sectioned like in cell-EM, but lie flat in a plane that is essentially perpendicular to the electron beam, hence their length can be systematically imaged. It was hence difficult to distinguish, within the cell environment, the true morphology (i.e., nanoparticles vs nanorods) of the nanostructures made by [2]OAc. In addition, it was curious to notice that no nanoparticle was observed in the lysosomes or cytoplasm at any time point investigated by cell-EM. Combined with the observed endocytotic uptake mechanism found by FACS analysis and the low co-localization of lysosome-target dyes and aggregated [2]OAc, these results suggested that this compound performed a direct transfer from the dynamine- and clathrin-coated vesicles to the mitochondria, avoiding the classical endosome- and lysosome-assisted endocytosis process.<sup>[31]</sup> All in all, the cell-EM images at three different time points fit quite well the time-dependent confocal microscopy images, demonstrating the formation, following endocytosis, of nanostructures of [2]OAc in the mitochondria, without involvement of the endosome or lysosome, and without nanoparticle formation (or migration) in the cytoplasm.

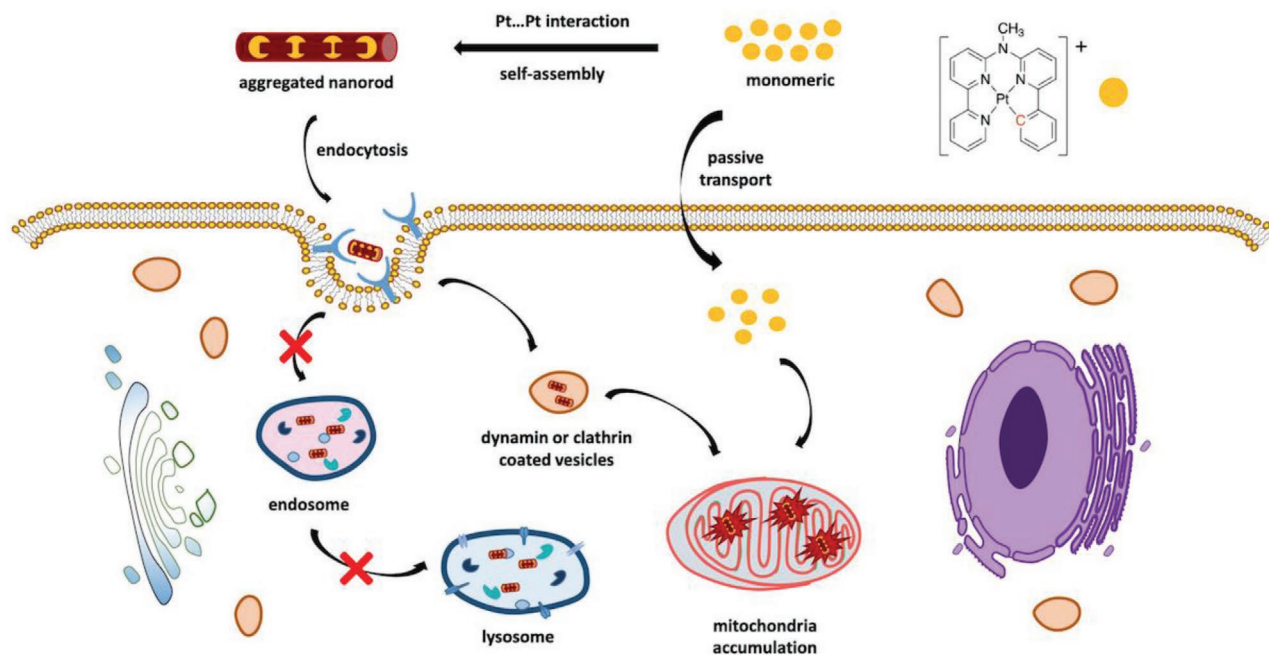
### 3. Discussion

In recent years, the metallophilic interaction between  $d^8$  or  $d^{10}$  metal complexes has developed as an essential form of

supramolecular interaction, with many applications in particular in the field of emitting solid-state materials or hydrogellators.<sup>[7,33]</sup> In a more biological context, our group recently demonstrated that the palladium analog of [1]OAc could serve as a very efficient PDT agent that generated serum-stabilized, phototoxic but not-emissive, nanorods via Pd...Pd metallophilic interactions.<sup>[21]</sup> These nanorods are difficult to study in cells because they are non-emissive. By altering the metal center to platinum, we now demonstrate that similar self-assembly takes place with [1]OAc and [2]OAc. Remarkably, the metallophilic Pt...Pt interaction at the source of the nanorod self-assembly in the serum-containing medium now generates deep-red emission, which allows for studying the uptake and intracellular fate of these nanorods both by confocal microscopy and cellular EM.

The results of the uptake inhibition experiments suggested that dynamin- and (or) clathrin dependent endocytosis, a specific uptake pathway working via dynamin and clathrin proteins, are the main channels for the nanoparticles of [1]OAc and [2]OAc to cross the cell membranes. However, near half of the Pt complexes [1]OAc and [2]OAc were internalized into the cells via passive diffusion (or at least energy-independent channels), suggesting that the platinum complexes might exist both as aggregated nanoparticles and isolated molecules in the cell medium. Importantly, already after 3 h, [2]OAc was found to locate in the mitochondria in an aggregated, emissive state. The confocal colocalization and cell-EM experiments excluded the role of lysosomes in the cellular movement of [2]OAc. These apparently conflicting results can be explained by a recent report that exogenous molecules may also traffic to mitochondria directly from the plasma membrane by clathrin-mediated endocytosis, and entry of the endosome into mitochondria using microtubule-dependent active transport.<sup>[31]</sup>

Overall, two (co-existing) mechanisms can be proposed to interpret the cellular uptake and time-dependent localization



**Scheme 1.** Schematic cellular uptake and movement of [2]OAc.

of [2]OAc. First, an energy-dependent mechanism can be proposed (**Scheme 1**): small nanoaggregates enter into cells via endocytosis, and traffic to the mitochondria directly via the clathrin- or dynamine-coated endosomes. These aggregates are small enough not to be detected by EM, but big enough to contribute to the phosphorescence signal detected by FACS. As a side note, this process is very fast and efficient, as it takes place within 3 h and leads to above half of the cellular uptake of the compound. The second mechanism involves passive uptake of [2]OAc as isolated molecules. These isolated molecules are invisible by cell EM and not emissive, but due to their positive charge they diffuse to the negatively charged mitochondrial membrane, where re-assembly occurs, contributing to the accumulation of larger and emissive nanoparticles in the mitochondria.

Whatever the mechanism for cellular uptake, Pt nanoparticles were observed in the mitochondria, suggesting that the Pt...Pt interaction is a reliable supramolecular interaction for building bioimaging platforms in cells, because it survives cell metabolism and even cell division. This interaction could be used for making supramolecular sensors or devices that can penetrate inside a cell by endocytosis, rearrange, and relocate to perform a specific function (here mitochondria staining). Importantly, these self-assembled sensors work at high wavelengths that are ideal for bioimaging. In the cell medium, these nanoaggregates are stabilized by plasma proteins, which generates nanorods, while in mitochondria they might have different, particle-like morphologies. Altogether, proteins, as well as salts, appear to play a critical role in balancing the repulsive (electrostatics) and attractive ( $\pi$ - $\pi$  stacking,  $d_z^2$  overlap) forces at the origin of the metallophilic interaction. The different proteins present in the cell medium, lysosome, cytosol, and mitochondria, may lead to different forms of self-assembly, which contributes to the

dynamics of the complex inside the cell. On the other hand, the structure of the platinum complex will also play an important role in the localization of the emitting self-assembly; recently, Lo, Yam et al published a platinum complex self-assembling in the nucleoli in the presence of RNA.<sup>[34]</sup>

#### 4. Conclusion

Cyclometalated platinum complexes are ideal structures for generating self-assembly via the metallophilic interaction. However, the balance between the hydrophobicity of the complexes and the strength of the metallophilic interaction, must be just right to allow controlled self-assembly of soluble nanostructures in a biological context. This work demonstrates that this balance can be found with the proper ligand set. It also highlights for the first time, the essential role played by serum proteins in the stabilization of the nanostructure generated by [1]OAc and [2]OAc in cell medium and living cells. Due to the exceptional photophysical properties of these aggregates, which not only absorb in the red and emit in the near-infrared region of the spectrum, but also show very low phototoxicity, long-term imaging of the aggregates was made possible, which allowed to follow their intracellular localization in time and study the up-to-now unraveled mechanism of cellular uptake. Because of their supramolecular aggregation properties, these compounds cross the cell membrane via a combination of passive uptake (for the monomers) and dynamine- and clathrin-dependent endocytosis (for the nanoparticles). The nanoparticles directly move to mitochondria via the specific dynamine- and clathrin-coated vesicles, and re-assemble inside the mitochondria as deep-red phosphorescent nanoparticles. It was quite fascinating to observe that these nanoparticles survive both in living

and dividing cells. Overall, this set of platinum complexes demonstrates exquisite perspectives for using the metallophilic interaction to build supramolecular nanosystems that can be used as deep-red trackers for different organelles – here the mitochondria.

## 5. Experimental Section

All the resource availability, materials availability, and experiment details are described in the electronic supporting information. The accession number for the crystal structure of [2]PF<sub>6</sub> in this paper is CCDC: 2001190.

## Supporting Information

Supporting Information is available from the Wiley Online Library or from the author.

## Acknowledgements

X.-Q.Z. gratefully acknowledges the China Scholarship Council (CSC) for a personal grant (No. 201606200045). This work is supported by the European Research Council via a Starting Grant to S.B. and a Huygens Fellowship Leiden University Grant to P.P. M.M. and D.H. acknowledge funding from the Fraunhofer Attract “3DNanoCell” grant. Dr. S. Zheng is thanked for the ICP-MS measurement. Prof. E. Bouwman is wholeheartedly acknowledged for scientific discussion and support. The cryo-EM measurements benefited from access to the Netherlands Centre for Electron Nanoscopy (NeCEN) at Leiden University.

## Conflict of Interest

The authors declare no conflict of interest.

## Author Contributions

X.-Q.Z. and S.B. contributed to the design of the molecules, experiments and methodology, and co-wrote the manuscript. X.Z. synthesized the molecules and made the characterization, photochemistry, aggregation analysis, and cytotoxicity experiments. M.M. and D.H. carried out the real-time confocal determination. Y.Z. helped with the design of cell uptake inhibition experiments. J.H. carried out the confocal colocalization experiments. Y.S. and F.B. carried out computational modeling. P.P. and A.K. performed the cryo-EM imaging of complexes in solution. L.Z. and M.H. prepared the samples and performed and analyzed EDX experiments, respectively. M.P.D. and A.M.B. performed and analyzed photophysical characterization (lifetime measurements, 77 K spectra, and emission quantum yields). M.A.S. performed the single crystal structure determination of [2]OAc. E.B. and R.I.K. performed cell EM imaging. All authors contributed to the reviewing and editing of the manuscript.

## Data Availability Statement

The data that support the findings of this study are available from the corresponding author upon reasonable request.

## Keywords

cyclometalation, electronic microscopy (EM), live cell imaging, nanoparticle, Pt...Pt metallophilic interaction, self-assembly

Received: December 21, 2020

Revised: June 27, 2021

Published online:

- [1] a) V. W. Yam, V. K. Au, S. Y. Leung, *Chem. Rev.* **2015**, *115*, 7589; b) A. Diez, J. Fornies, C. Larraz, E. Lalinde, J. A. Lopez, A. Martin, M. T. Moreno, V. Sicilia, *Inorg. Chem.* **2010**, *49*, 3239; c) Y. S. Wong, M. C. Tang, M. Ng, V. W. Yam, *J. Am. Chem. Soc.* **2020**, *142*, 7638; d) M. A. Soto, V. Carta, R. J. Andrews, M. T. Chaudhry, M. J. MacLachlan, *Angew. Chem., Int. Ed.* **2020**, *59*, 10348; e) S. S. Tang, C.-P. Chang, I. J. B. Lin, L.-S. Liou, J.-C. Wang, *Inorg. Chem.* **1997**, *36*, 2294; f) M. A. Rawashdeh-Omary, M. A. Omary, H. H. Patterson, J. P. Fackler, *J. Am. Chem. Soc.* **2001**, *123*, 11237; g) M. A. Rawashdeh-Omary, M. A. Omary, H. H. Patterson, *J. Am. Chem. Soc.* **2000**, *122*, 10371.
- [2] W. Lu, Y. Chen, V. A. Roy, S. S. Chui, C. M. Che, *Angew. Chem., Int. Ed.* **2009**, *48*, 7621.
- [3] A. Aliprandi, D. Genovese, M. Mauro, L. De Cola, *Chem. Lett.* **2015**, *44*, 1152.
- [4] a) J. Romanova, M. R. Ranga Prabhat, P. D. Jarowski, *J. Phys. Chem.* **2016**, *120*, 2002; b) M. Y. Yuen, V. A. Roy, W. Lu, S. C. Kui, G. S. Tong, M. H. So, S. S. Chui, M. Muccini, J. Q. Ning, S. J. Xu, C. M. Che, *Angew. Chem., Int. Ed.* **2008**, *47*, 9895; c) X. Yan, T. R. Cook, P. Wang, F. Huang, P. J. Stang, *Nat. Chem.* **2015**, *7*, 342; d) H. L. Au-Yeung, S. Y. Leung, A. Y. Tam, V. W. Yam, *J. Am. Chem. Soc.* **2014**, *136*, 17910; e) A. Aliprandi, M. Mauro, L. De Cola, *Nat. Chem.* **2016**, *8*, 10; f) S. Marpu, P. K. Upadhyay, D. T. Nguyen, I. W. Oswald, R. K. Arvapally, R. A. Petros, Z. Hu, M. A. Omary, *J. Phys. Chem. C* **2015**, *119*, 12551.
- [5] K. Li, G. S. Ming Tong, Q. Wan, G. Cheng, W. Y. Tong, W. H. Ang, W. L. Kwong, C. M. Che, *Chem. Sci.* **2016**, *7*, 1653.
- [6] a) H. Xiang, J. Cheng, X. Ma, X. Zhou, J. J. Chruma, *Chem. Soc. Rev.* **2013**, *42*, 6128; b) M. Li, W.-H. Chen, M.-T. Lin, M. A. Omary, N. D. Shepherd, *Org. Electron.* **2009**, *10*, 863; c) J. W. Schindler, R. C. Fukuda, A. W. Adamson, *J. Am. Chem. Soc.* **1982**, *104*, 3596; d) W. Kirmse, K. Kund, *J. Am. Chem. Soc.* **1989**, *111*, 1465.
- [7] M. Mauro, A. Aliprandi, D. Septiadi, N. S. Kehr, L. De Cola, *Chem. Soc. Rev.* **2014**, *43*, 4144.
- [8] M. J. Miller, S. H. Wei, I. Parker, M. D. Cahalan, *Science* **2002**, *296*, 1869.
- [9] a) N. A. Smith, P. J. Sadler, *Philos. Trans. R. Soc., A* **2013**, *371*, 20120519; b) C. Ash, M. Dubec, K. Donne, T. Bashford, *Lasers Med. Sci.* **2017**, *32*, 1909.
- [10] D. Septiadi, A. Aliprandi, M. Mauro, L. De Cola, *RSC Adv.* **2014**, *4*, 25709.
- [11] J. L. Tsai, T. Zou, J. Liu, T. Chen, A. O. Chan, C. Yang, C. N. Lok, C. M. Che, *Chem. Sci.* **2015**, *6*, 3823.
- [12] a) C.-K. Koo, B. Lam, S.-K. Leung, M. H.-W. Lam, W.-Y. Wong, *J. Am. Chem. Soc.* **2006**, *128*, 16434; b) C. Y.-S. Chung, S. P.-Y. Li, M.-W. Louie, K. K.-W. Lo, V. W.-W. Yam, *Chem. Sci.* **2013**, *4*, 2453; c) L. Y. Liu, H. Fang, Q. Chen, M. H. Chan, M. Ng, K. W. Wang, W. Liu, Z. Tian, J. Diao, Z. W. Mao, V. W. W. Yam, *Angew. Chem., Int. Ed.* **2020**, *59*, 19229.
- [13] a) N. Metzler-Nolte, Z. Guo, *Dalton Trans.* **2016**, *45*, 12965; b) X. Wang, X. Wang, S. Jin, N. Muhammad, Z. Guo, *Chem. Rev.* **2019**, *119*, 1138.
- [14] N. Cutillas, G. S. Yellol, C. de Haro, C. Vicente, V. Rodríguez, J. Ruiz, *Coord. Chem. Rev.* **2013**, *257*, 2784.

- [15] a) S. C. Kui, F. F. Hung, S. L. Lai, M. Y. Yuen, C. C. Kwok, K. H. Low, S. S. Chui, C. M. Che, *Chem. - Eur. J.* **2012**, *18*, 96; b) L. J. Chen, H. B. Yang, *Acc. Chem. Res.* **2018**, *51*, 2699; c) M. L. Saha, X. Yan, P. J. Stang, *Acc. Chem. Res.* **2016**, *49*, 2527; d) C. N. Lok, T. Zou, J. J. Zhang, I. W. Lin, C. M. Che, *Adv. Mater.* **2014**, *26*, 5550.
- [16] a) W. Zhang, M. Wang, W. Tang, R. Wen, S. Zhou, C. Lee, H. Wang, W. Jiang, I. M. Delahunty, Z. Zhen, H. Chen, M. Chapman, Z. Wu, E. W. Howerth, H. Cai, Z. Li, J. Xie, *Adv. Mater.* **2018**, *30*, 1805557; b) L. Cheng, C. Wang, L. Feng, K. Yang, Z. Liu, *Chem. Rev.* **2014**, *114*, 10869.
- [17] B. Yang, Y. Chen, J. Shi, *Chem* **2018**, *4*, 1284.
- [18] a) H. Kang, S. Hu, M. H. Cho, S. H. Hong, Y. Choi, H. S. Choi, *Nano Today* **2018**, *23*, 59; b) D. M. Samhadaneh, G. A. Mandl, Z. Han, M. Mahjoob, S. C. Weber, M. Tuznik, D. A. Rudko, J. A. Capobianco, U. Stochaj, *ACS Appl. Bio Mater.* **2020**, *3*, 4358; c) Y. Feng, H. Chen, Y. Wu, I. Que, F. Tamburini, F. Baldazzi, Y. Chang, H. Zhang, *Biomaterials* **2020**, *230*, 119637; d) M. Buchner, P. Garcia Calavia, V. Muhr, A. Kroninger, A. J. Baeumner, T. Hirsch, D. A. Russell, M. J. Marin, *Photochem. Photobiol. Sci.* **2019**, *18*, 98.
- [19] J. Zhao, M. H. Stenzel, *Polym. Chem.* **2018**, *9*, 259.
- [20] a) J. Chen, J. Li, J. Zhou, Z. Lin, F. Cavalieri, E. Czuba-Wojnilowicz, Y. Hu, A. Glab, Y. Ju, J. J. Richardson, F. Caruso, *ACS Nano* **2019**, *13*, 11653; b) S. Behzadi, V. Serpooshan, W. Tao, M. A. Hamaly, M. Y. Alkawareek, E. C. Dreaden, D. Brown, A. M. Alkilany, O. C. Farokhzad, M. Mahmoudi, *Chem. Soc. Rev.* **2017**, *46*, 4218.
- [21] X. Q. Zhou, M. Xiao, V. Ramu, J. Hilgendorf, X. Li, P. Papadopoulos, M. A. Siegler, A. Kros, W. Sun, S. Bonnet, *J. Am. Chem. Soc.* **2020**, *142*, 10383.
- [22] X. Q. Zhou, A. Busemann, M. S. Meijer, M. A. Siegler, S. Bonnet, *Chem. Commun.* **2019**, *55*, 4695.
- [23] S. Sinn, L. Yang, F. Biedermann, D. Wang, C. Kübel, J. J. L. M. Cornelissen, L. De Cola, *J. Am. Chem. Soc.* **2018**, *140*, 2355.
- [24] S. Marpu, P. K. Upadhyay, D. T. Nguyen, I. W. H. Oswald, R. K. Arvapally, R. A. Petros, Z. Hu, M. A. Omary, *J. Phys. Chem. C* **2015**, *119*, 12551.
- [25] V. H. S. van Rixel, A. Busemann, M. F. Wissingh, S. L. Hopkins, B. Siewert, C. van de Griend, M. A. Siegler, T. Marzo, F. Papi, M. Ferraroni, P. Gratteri, C. Bazzicalupi, L. Messori, S. Bonnet, *Angew. Chem., Int. Ed.* **2019**, *58*, 9378.
- [26] K. W. Dunn, M. M. Kamocka, J. H. McDonald, *Am. J. Physiol. Cell Physiol.* **2011**, *300*, C723.
- [27] C. A. Puckett, R. J. Ernst, J. K. Barton, *Dalton Trans.* **2010**, *39*, 1159.
- [28] a) J. Yang, J. Tu, G. E. M. Lamers, R. C. L. Olsthoorn, A. Kros, *Adv. Healthcare Mater.* **2017**, *6*, 1700759; b) D. Dutta, C. D. Williamson, N. B. Cole, J. G. Donaldson, *PLoS One* **2012**, *7*, e45799; c) G. Preta, J. G. Cronin, I. M. Sheldon, *Cell Commun. Signaling* **2015**, *13*, 24.
- [29] a) O. Harush-Frenkel, N. Debotton, S. Benita, Y. Altschuler, *Biochem. Biophys. Res. Commun.* **2007**, *353*, 26; b) T.-G. Iversen, T. Skotland, K. Sandvig, *Nano Today* **2011**, *6*, 176.
- [30] E. M. M. Manders, F. J. Verbeek, J. A. Aten, *J. Microsc.* **1993**, *169*, 375.
- [31] Z. Wei, W. Su, H. Lou, S. Duan, G. Chen, *J. Mol. Cell. Biol.* **2018**, *10*, 539.
- [32] Z. Zolmajd-Haghighi, Q. S. Hanley, *Biophys. J.* **2014**, *106*, 1457.
- [33] a) Z. Gao, P. A. Korevaar, R. Zhong, Z. Wu, F. Wang, *Chem. Commun.* **2018**, *54*, 9857; b) Z. Gao, Y. Han, Z. Gao, F. Wang, *Acc. Chem. Res.* **2018**, *51*, 2719; c) L. Barrientos, S. Miranda-Rojas, F. Mendizabal, *Int. J. Quantum Chem.* **2018**, *119*, e25675; d) Q. Wan, W.-P. To, X. Chang, C.-M. Che, *Chem* **2020**, *6*, 945; e) X. Yin, S. A. Warren, Y. T. Pan, K. C. Tsao, D. L. Gray, J. Bertke, H. Yang, *Angew. Chem., Int. Ed.* **2014**, *53*, 14087; f) V. W.-W. Yam, V. K.-M. Au, S. Y.-L. Leung, *Chem. Rev.* **2015**, *115*, 7589; g) Y. Han, Z. Gao, C. Wang, R. Zhong, F. Wang, *Coord. Chem. Rev.* **2020**, *414*, 213300; h) Z. Gao, P. A. Korevaar, R. Zhong, Z. Wu, F. Wang, *Chem. Commun.* **2018**, *54*, 9857; i) A. Kishimura, T. Yamashita, T. Aida, *J. Am. Chem. Soc.* **2005**, *127*, 179; j) J. C. Lima, L. Rodríguez, *Inorganics* **2015**, *3*, 1.
- [34] A. S.-Y. Law, L. C.-C. Lee, K. K.-W. Lo, V. W.-W. Yam, *J. Am. Chem. Soc.* **2021**, *143*, 5396.